



Local axis orientation mapped by polarization sensitive optical coherence tomography provides a unique contrast to identify caries lesions in enamel

PEIJUN TANG,¹ NHAN LE,¹ JIE LU,¹  KWOK-HUNG CHUNG,² HREBESH SUBHASH,³ LATONYA KILPATRICK-LIVERMAN,³ AND RUIKANG K. WANG^{1,*} 

¹Department of Bioengineering, University of Washington, 3720 15th Ave NE, Seattle, WA 98195, USA

²Department of Restorative Dentistry, University of Washington, Seattle, WA, 98195, USA

³Clinical Method Development – Oral Care, Colgate-Palmolive Company, Piscataway, New Jersey, USA
*wangrk@uw.edu

Abstract: Due to rod-like hydroxyapatite crystal organizations, dental enamel is optically anisotropic, i.e., birefringent. Healthy enamel is known to be intrinsically negatively birefringent. However, when demineralization of enamel occurs, a considerable number of inter-crystallite spaces would be created between the crystallites in the enamel, which could lead to a sign reversion in birefringence of the enamel structure. We propose that this sign reversion can be leveraged in polarization sensitive OCT (PSOCT) imaging to differentiate early caries lesions from healthy enamel. In this study using PSOCT, we first confirm that the change in birefringence sign (negative to positive) can lead to a 90-degree alteration in the local axis orientation because of the switch between the fast and slow optic axes. We then demonstrate, for the first time, that the local axis orientation can be utilized to map and visualize the WSLs from the healthy enamel with a unique contrast. Moreover, the sharp alteration in local axis orientation gives a clear boundary between the WSLs and the healthy enamel, providing an opportunity to automatically segment the three-dimensional WSLs from the healthy enamel, enabling the characterization of their size and depth information in an intuitive way, which may aid clinical decision making and treatment planning.

© 2022 Optica Publishing Group under the terms of the [Optica Open Access Publishing Agreement](#)

1. Introduction

White spot lesions (WSLs) or early caries lesions in enamel are a clinically detectable sign of demineralization. Their presence is a topic of considerable interest in dentistry because they are clearly visible and represent an early, reversible stage of the caries process [1]. Formation of caries lesions is a dynamic process that, if detected early, can be effectively prevented, arrested or reversed by proper treatments [2]. Therefore, the characterization and understanding of the properties of WSLs would provide a more critical basis in the assessment of the repair potential for caries.

One of the most influential contributions to the field of caries pathology came from the interpretation of birefringence of enamel under polarization light microscopy (PLM) [1,3–7], where sound enamel is found to be negatively intrinsic birefringent due to the morphologically aligned mineral nanocrystals (or rods) orthogonal to the surface. Yet, their arrangement in the surrounding matrix leads to form birefringence with a positive sign, competing with the intrinsic birefringence. During the demineralization process, a considerable number of inter-crystallite spaces form between the crystallites. These spaces, containing air or liquid with lower refractive index, lead to decreased volume fraction of the rods that would increase the form birefringence, which competes with the intrinsic birefringence, and eventually reverses the birefringence sign

in the lesions [1,3–7]. Thus, this sign change in the birefringence could become one of the important features that can be used to differentiate demineralized enamel from healthy enamel. Although this birefringent phenomenon has been investigated using the PLM technique, all of the previous investigations were based on sectioned enamel because 1) the lesions are below the enamel surface, and 2) the PLM is not a depth-resolved imaging method. Clearly, the requirement of these destructive procedures limits the PLM's applications to in vivo or in vitro study investigations of non-sectioned human teeth.

Being a non-invasive optical imaging modality, polarization sensitive optical coherence tomography (PSOCT) [8–20] utilizes the polarized probing light and the polarization diverse detection scheme to provide depth-resolved birefringent information of the sample with high resolution and without the requirement of destructive procedures. Taking advantage of its non-invasive 3D imaging capability, PSOCT has been utilized to study WSLs in vitro or in vivo in several studies [21–25]. Since enamel demineralization increases multiple scattering of the light, the polarization states of the light can vary in the WSL and caries. Based on this mechanism, these previous studies were mainly focused on the variations in the polarization state of the light in WSLs. Both degree of polarization uniformity (DOPU) and the intensity difference between the orthogonal polarization channels (also called cross-polarization OCT) were developed to represent the variations in the polarization state, which has been leveraged to characterize demineralized enamel [21–24]. However, it is difficult for these two parameters to provide depth-resolved information. This is because the polarization states of the light scattered back from the deeper location can be modulated by the multiple scattering of the tissue on top of it. This modulation gives rise to erroneous measurements (underestimations) of DOPU at the deeper locations even when there is no demineralized tissue, which can lead to the misinterpretation of the structure or composition within the sample, i.e. low specificity, and would limit applicability to clinical decision making. To characterize and interpret the WSLs at different depths without ambiguity, localized (i.e., depth resolved) PSOCT measurements are needed, which are yet to be demonstrated.

Local axis orientation is one of the depth-resolved parameters that can be provided by PSOCT imaging, which shows the orientation of the optic axis of the sample at each depth. More importantly, local axis orientation is sensitive to the sign of the birefringence of the sample, one of the important features in the WSLs as mentioned above. A sign reversion in the sample represents a switch between the fast and slow axis. Hence, the sign reversion can be presented as a 90-degree alteration in the optic axis measurement. We propose that this sharp change in the local axis orientation can be leveraged in the PSOCT imaging to contrast and segment the positive birefringent WSLs from the healthy enamel, which exhibits negative birefringence. To support our hypothesis, we utilized a PSOCT system to map the local phase retardation and local axis orientation that are then used to characterize both the artificial (created in vitro) and natural WSLs in enamel. In this paper, we first investigated the change in local phase retardation and local axis orientation of the artificially produced WSLs in bovine samples under the PSOCT and demonstrated that local axis orientation provides a unique contrast to map white spot lesions. Then we generalized this methodology for identifying naturally formed WSLs in human enamel and cross-validated the method with the gold standard histological approach. Finally, we demonstrated that the utilization of the local axis orientation information can automatically segment WSLs from healthy enamel, providing a unique opportunity to visualize the 3D skeleton of the WSLs, which may help dentists to more effectively plan treatments.

2. Methods and materials

2.1. PSOCT system setup

The PSOCT system (Fig. 1) employed in this study has previously been described in detail [14,26]. In short, the system used a 1310 nm swept-source laser (SL1310V1-10048, Thorlabs) with a

spectral tuning range of 100 nm and 100 kHz A-line rate, giving an approximate axial resolution of $\sim 7.5 \mu\text{m}$ in air. The polarization-sensitive imaging was realized by a single polarization input configuration, in which the sample is illuminated by a circularly polarized light and the probing lights at the two orthogonal polarized channels backscattered from the sample are detected. In the imaging probe, an f-theta telecentric scanning objective lens (LSM03, Thorlabs, USA) was deployed to deliver the probing light to and from the sample, which provides an approximate spot size/lateral resolution of $25 \mu\text{m}$. The light energy impinging on the sample was measured to be $\sim 5\text{mW}$. To characterize the optical properties of the sample, the detected signals from the two channels were used to reconstruct two typical OCT structural images using Fourier transformation [27]. Based on the intensities and the phase difference between these two structural images, the Stokes parameters of Q, U and V were obtained and mapped. Then a 6×6 spatial average was applied to each Stokes parameter image to obtain the DOPU image with enhanced signal to noise ratio (SNR) [28]. Finally, the local phase retardation and local axis orientation were reconstructed based on the Stokes parameters Q, U and V by using a discrete differential geometry (DDG) based polarization state tracing (PST) method proposed in the previous study [14,29].

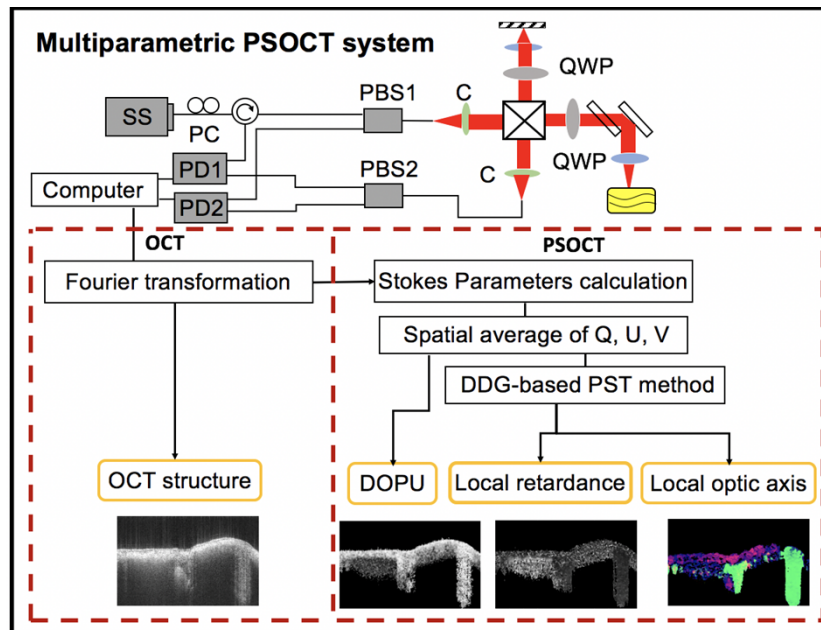


Fig. 1. Schematic of the PSOCT system used in this study. SS: swept source laser; PC: polarization controller; OC: optical circulator; PBS: polarization beam splitter; QWP: quarter wave plate; PD: photo detector. Below the system schematic is a data processing flow chart of the computations of the multiple parameters for the traditional OCT results and the PSOCT results. DOPU: degree of polarization uniformity. DDG-based PST method: discrete differential geometry-based polarization state tracing method.

2.2. Signal processing

Multiple parameters can be provided concurrently in one single volume scan using the PSOCT system described above. These images can be divided into two groups: 1) OCT intensity image. This group is utilized to guide and cross-validate the polarization results. 2) the second group includes those that are derived from polarization-related measurements, including DOPU, local

phase retardation and local axis orientation images. The results from this latter group are for the further investigations of the birefringent properties of the WSLs in enamel.

To obtain the structural image, conventional OCT processing procedures [30] are applied to the interference signals obtained from both horizontal and vertical channels that result in complex, depth-resolved A-scans with amplitudes $A_{H,V}(z)$ and phases $\phi_{H,V}(z)$. The structural OCT image $I(z)$ can therefore be obtained by:

$$I(z) \propto A_H(z)^2 + A_V(z)^2, \quad (1)$$

All the polarization related derivations in this study are computed based on the Stokes parameters (I, Q, U, V), which are obtained by

$$S = \begin{pmatrix} I \\ Q \\ U \\ V \end{pmatrix} = \begin{pmatrix} A_H(z)^2 + A_V(z)^2 \\ A_H(z)^2 - A_V(z)^2 \\ 2A_H(z)A_V(z)\cos(\phi_H(z) - \phi_V(z)) \\ 2A_H(z)A_V(z)\sin(\phi_H(z) - \phi_V(z)) \end{pmatrix}, \quad (2)$$

The degree of polarization uniformity DOPU is obtained as [28]:

$$DOPU = \sqrt{Q_m^2 + U_m^2 + V_m^2}, \quad (3)$$

where the indices m indicates the averaged Stokes vector elements over the adjacent pixels. Here, we used 6×6 spatial averaged filter to smooth the images to arrive SNR-enhanced results.

To obtain the phase retardation and axis orientation information, the averaged Stokes parameters (6×6 spatial averaging filter) are normalized to the Poincare sphere's surface. The trajectory of the Stokes vectors in each A-scan at the Poincare sphere is considered as a spatial curve. Discrete differential geometry (DDG) is applied to this curve to provide the TNB vectors (T: tangent vector, N: normal vector, B: binormal vector of the curve) as described in [14,29]. Based on the TNB vectors of this curve, the local phase retardation δ_n and local axis orientation A_n at the n -th pixel in depth can be obtained by [14,29]:

$$\delta_n = \frac{1}{2} \arccos \frac{N_{n-1} \cdot N_n}{|N_{n-1}| |N_n|}. \quad (4)$$

$$A_n = R_{n-1}(-\delta_{n-1}; A_{n-1}) R_{n-2}(-\delta_{n-2}; A_{n-2}) \dots R_1(-\delta_1; A_1) B_n, \quad (5)$$

where N_n , B_n are the normal and binormal vector of the spatial curve, $R_n(-\delta_n; A_n)$ is the 3D rotation matrix determined by A_n and $-\delta_n$.

2.3. Ex-vivo bovine enamel block with artificial white spot lesions

We first used artificially generated white spot lesions in bovine enamel samples to describe the PSOCT measurements and confirm the depth-resolved sign reversion in the birefringence in WSL as compared to sound enamel. To induce the WLS, we followed a standard procedure [31]. The bovine sample was flattened, cut and polished to generate a $4 \times 4 \times 3$ mm block (Fig. 2(A)). The block consisted of approximately $4 \times 4 \times 1.5$ mm³ enamel and $4 \times 4 \times 1.5$ mm³ dentin. Half of the block ($2 \times 4 \times 3$ mm³) was then coated with acid-resistant varnish as a control treatment, and the other half $2 \times 4 \times 3$ mm³ block was exposed to a pH-cycling regimen [31]. The block was immersed into a demineralizing solution (0.05N acetic acid hydroxyethyl-cellulose gel) for 16 hours, and then allowed to re-mineralize in remin-solution (calcium chloride dihydrate, potassium dihydrate phosphate and potassium chloride with HEPEs as buffer) for another 8 hours. This pH cycling

process continued over a period of 3 days so that artificially induced WSLs (about 0.3 mm in thickness) were generated at the treatment site (Fig. 2(B)). The demineralization/remineralization cycle was conducted to generate sub-surface lesions. The block was then stored in distilled water in preparation for use for PSOCT imaging. The imaging field of view (FOV) was 5 mm x 5 mm with 500 x 500 pixels.

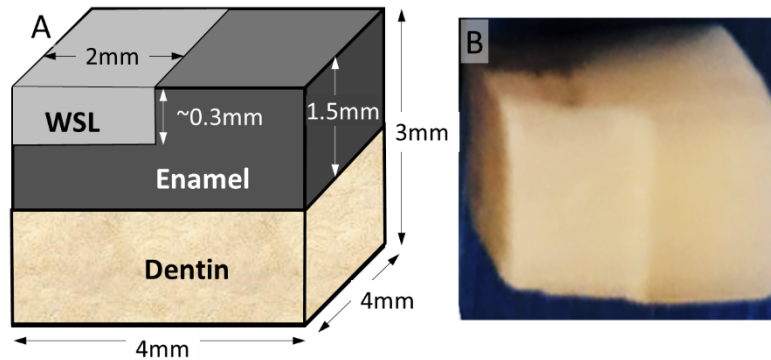


Fig. 2. Bovine enamel block with artificially generated white spot lesions. (A) schematic illustration of the enamel block containing enamel (top half) and dentin (bottom half) with approximate size dimensions as shown. The artificially generated WSLs are located at the superficial layer of the left side of the block with a depth of about 0.3 mm. (B) Photograph taken by viewing the block from the top with the WSL facing up, where the region of WSLs is indicated by the whitish color.

2.4. Extracted human tooth samples with natural white spot lesions

In order to demonstrate the feasibility of contrasting WSLs and caries in human enamel with PSOCT, we selected ex-vivo tooth samples with ICDAS scores of 2 [32], where ICDAS is an international system for caries detection and assessment. ICDAS 2 represents the early lesions (both caries and WSLs) that can be arrested and reversed. The tooth samples were obtained from the University of Washington dental school. They were being used for educational purposes. The teeth were stored in 0.5% sodium hypochlorite disinfectant prior to their selection. The white spot lesions on the tooth were then identified, selected, marked and scored by a dental expert trained and calibrated in the use of ICDAS. The PSOCT scan was performed with the buccal surface facing the OCT beam. The imaging FOV of the scan was 6 mm x 6 mm with 500 x 500 pixels. After PSOCT imaging, a plane of sectioning was determined that was parallel to the occlusal surface, purposely covering both the white-spot lesion and healthy enamel for the validation of the PSOCT imaging results. We used a typical dental model trimmer for the sectioning of the tooth. When the sectioning plane touched the white spot lesions, we hand-sanded the tooth with 500-grit and progressively to 1000-grit sandpapers to achieve a uniform and smooth surface, ready for PSOCT scan. The second PSOCT scan was then performed with the sectioning plane facing the laser beam. The imaging FOV was 3 mm x 3 mm with 500 x 500 pixels.

After PSOCT imaging, we exposed the sectioned tooth with a disclosing agent (FP-SCHEIN-193, Henry Schein Inc., p/n: 1024453) for a period of 15 seconds to stain the WSLs for the purpose of validating the PSOCT results. The sectioned tooth was then cleaned and air-dried, observed under a light microscope (AMScope, 0.5X objective lens, 30mm WF10X/20 eyepiece). In this way, the WSLs would be stained by the agent and appear green in color. The LED illumination was set to max, and white/black balance was applied. The microscopic images of the stained WSL were then used as the standard to compare with the second PSOCT results.

To demonstrate the segmentation of WSLs using local optic axis orientation information in Section 3.2.3, a separate tooth with naturally formed caries was imaged with PSOCT at the interproximal surface of the tooth. The imaging FOV was 6 mm x 6 mm with 500 x 500 pixels.

3. Results

3.1. PSOCT of artificially generated subsurface white spot lesions in bovine enamel

To investigate the depth-resolved birefringent properties of WSLs in enamel, a bovine enamel block with artificially produced WSLs at the superficial layer (See Section 2.3, Fig. 2) was imaged by the PSOCT system. The cross-sectioned images (Figs. 3(A)–3(D)) at the region indicated by the black dash line in the photograph in Fig. 3(A) were selected. In the cross-sectioned intensity image (Fig. 3(A)), the WSL is visualized as a brighter scattering region with a measured thickness of $\sim 250\ \mu\text{m}$ (as indicated by the arrows) at the left side of the enamel block, showing that the WSL was artificially produced at the superficial layer of the enamel while the enamel below was not affected.

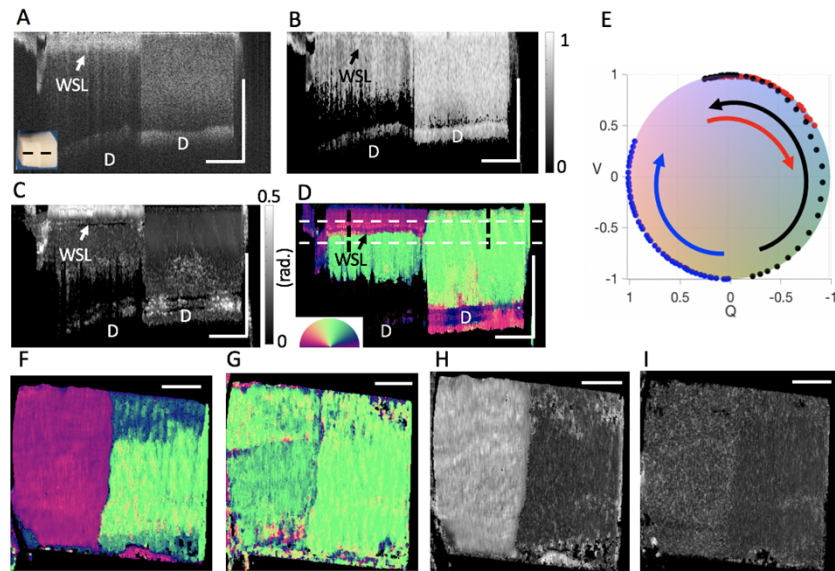


Fig. 3. PSOCT imaging of the bovine enamel block with artificially produced WSLs. PSOCT cross-sectional images of (A) scattering intensity (i.e., typical OCT B-scan), (B) DOPU, (C) local phase retardation and (D) local axis orientation derived from the bovine enamel block, respectively. (E) The trajectories of the output polarization states in two depth positions with a depth extent of $400\ \mu\text{m}$ (indicated by the black dash lines in the cross-sectional image in D) on the Poincaré sphere. The trace path indicated by the blue points represents the output polarization states scattered back from the sound enamel (at the depth position indicated by the black dash line on the right in D) while the black and red points represent the trace path scattered back from the WSLs (indicated by the black dash line on the left in D). (F) and (G) The *en face* local axis orientation images of the bovine enamel at depth of $150\ \mu\text{m}$ and $400\ \mu\text{m}$ below the surface respectively. (H) and (I) The *en face* local phase retardation images of the bovine enamel at depth of $150\ \mu\text{m}$ and $400\ \mu\text{m}$ below the surface respectively. The scale bar = 1 mm.

The strong scattering of the WSL would be responsible for introducing depolarization to the probing light (Fig. 3(B)), where the DOPU values are lower than 1 (mean DOPU: ~ 0.72) in the left half of the bovine enamel. However, unlike the scattering image, it is difficult for DOPU to

differentiate the WSL from the sound enamel that is located right below it, as the light scattered back from the deeper healthy layer is also depolarized (or modulated) by the demineralized enamel above. On the contrary, the WSLs and the sound enamel below it can be differentiated clearly in the local phase retardation (Fig. 3(C)) and local axis orientation (Fig. 3(D)) images, due to their depth-resolved ability. An increase in local phase retardation was observed (white arrows in Fig. 3(C)) at the WSL, and more importantly there is an approximate 90° transition in axis orientation at the junction between the WSL and the sound enamel just below it (Fig. 3(D)). This phenomenon demonstrates the reversion of the birefringence sign effect in the enamel, which provides a distinct and unique contrast in PSOCT to unambiguously differentiate the WSLs from the healthy enamel.

To interpret the 90° transition in the axis orientation in the WSLs with respect to the sound enamel, we visualized the trajectories of the output polarization states in the A-scans from the surface to the depth of $\sim 400\ \mu\text{m}$ on the Poincare sphere in Fig. 3(E), where the blue points represent the pixels along the depth direction at the sound enamel as indicated by the right black dashed vertical-line in Fig. 3(D), and the black points and then the red points are those pixels across the WSLs as indicated by the left black dashed vertical-line in Fig. 3(D).

For the light scattered back from the sound enamel, with the increase of the depth, the polarization states rotated clockwise (as indicated by the blue arrow in Fig. 3(E)) about a constant axis, forming a circular curve (as indicated by the blue points). Since the rotation axis (defined by the right-hand rule) of the output polarization state represents the optic axis of the sample, the relatively uniform orientation of the rotation axis in the A-scan indicates a homogenous alignment of the enamel rods along depth. The local phase retardation, being the rotation angle, is relatively small between the adjacent output polarization states (2.3 degree/pixel in this sample), suggesting that the phase retardation of the sound enamel is relatively weak.

The output polarization states are scattered back at the positions covering the WSLs (indicated by the black points in Fig. 3(D)), rotated about the same axis but in an opposite direction as shown in the black arrow, making the orientation of the WSLs to appear $\sim 90^\circ$ relative to the sound enamel. The rotation angle at the WSLs is also larger (measured at ~ 8.1 degree/pixel) than that in the sound enamel, indicating that the WSLs have a higher local phase retardation than the sound enamel. With the increase of depth beyond the WSLs, the output polarization states (indicated by the red points) rotated clockwise about the axis again (indicated by the red arrow) by a smaller rotation angle (estimated at ~ 1.9 degree/pixel, a value similar to the measured value at the sound enamel on the right side of the sample), revealing that the hard tissues below the WSLs are the sound enamel. There are two factors that can cause this transition in axis orientation: 1) the alignment of the sample rotates physically 90° in the cartesian coordinate system (which is not the case in the current study); and 2) the refractive index in the sample changes and reverses the birefringence sign. In the latter case, the fast and slow axes of the sample would switch and cause a 90° transition. According to the previous studies [1,3–8] involving polarization microscopy, it was found that WSLs can cause the reversion of the birefringence sign. Hence, we conclude that the 90° transition in the axis orientation in the WSLs is responsible for the reversion of the birefringence sign.

Figures 3(F)–3(I) respectively show the *en face* images selected at 2 different depths ($150\ \mu\text{m}$ and $400\ \mu\text{m}$ from the surface) of the enamel block by using local axis orientation and local phase retardation as the imaging parameters. The local axis orientation and local phase retardation visualize the artificially produced WSLs as shown in Fig. 3(F) and 3(H), which are at the depth of $150\ \mu\text{m}$ below the surface. In the *en face* images at depth of $400\ \mu\text{m}$ (Fig. 3(G) and 3(I)), both sides of the enamel were healthy, demonstrating that the local axis orientation and local phase retardation can mitigate the problem induced by the accumulation effect when using the DOPU as the imaging contrast. While the results presented here were from a single sample, we confirmed that this conclusion holds for all the artificially WSL-induced samples ($N = 8$) that

were imaged. These experiments demonstrate that the local axis orientation presents a unique contrast mechanism to map the WLSs in the enamel. It should be noted that the value of the local axis orientation in this study does not represent the absolute orientations of the enamel rods. This is because the PSOCT can only measure the projection of the sample's actual axis orientation onto the plane that is orthogonal to the direction of the incident light due to the round-trip measurement. Although the value of the axis orientation is relative, the sharp change in the orientation is absolute, which can indicate the change of the birefringence sign. Since the switch of the birefringence sign is our focus in this study, the absolute values of the axis orientation are less relevant. To present the results, we calibrated the orientation of the sound enamel to be 90° (i.e., the green color) by rotating the corresponding coordinate system in all the axis orientation images.

3.2. Naturally formed WSLs in human enamel

Next, we used the PSOCT system to study naturally formed WSLs in extracted human teeth (as shown in the photograph in Fig. 5(A)). The *ex vivo* WSL samples here resemble the condition of many early caries of *in vivo* human. We used the *ex vivo* WSL samples to demonstrate the potential feasibility of detecting *in vivo* early caries.

3.2.1. PSOCT results on ex-vivo tooth and histology validation

To demonstrate the feasibility of PSOCT for *in vivo* WSL and caries, the human tooth described in Section 2.4 was sectioned along the occlusal plane. The tooth was then stained by a disclosing agent, which visualizes the WSLs as a green color under the white light microscope. Figures 4(A)–4(D) show the photograph of the stained sectioned enamel and the corresponding *en face* scattering intensity, local phase retardation and local axis orientation images, respectively. The *en face* images in Figs. 4(B)–4(D) are at the depth of $30\ \mu\text{m}$. In the photograph of the stained sectioned enamel (Fig. 4(A)), the WSLs are visualized as the green color. These WSLs are presented as brighter signals in the OCT intensity image (Fig. 4(B)) with higher phase retardation (Fig. 4(C)) in the corresponding images as expected, validating the ability of these parameters to contrast the WSLs. In the local axis orientation image (Fig. 4(D)), the axis orientation of the healthy enamel (unstained regions) reveals the direction of the enamel rods, which is almost orthogonal to the surface of the enamel. This observation is consistent with previous histological studies [33]. However, the orientation values in the WSLs are distinct, and approximately orthogonal to the healthy enamel below the WSLs, along the radial axis. This indicates the sign of the birefringence has been reversed in the WSLs. The distinct contour of the WSLs in Fig. 4(D) is consistent with the stained results, indicating that local axis orientation can also be used to visualize the naturally formed WSLs in human teeth; and the sharp transition in the measured local optic axis along the radial axis of the tooth would establish the boundary between the WSL and healthy enamel, correlating with the histology WSL/enamel boundary. We will use this knowledge in the subsequent experiments to identify the WSL and healthy enamel. It should be noted that the boundary may be slightly changed by the refractive index of the immersion media.

3.2.2. Local axis orientation as an indicator to uniquely contrast WSLs

A sharp transition in the local axis orientation ($\sim 90^\circ$) in WSLs from the healthy enamel as mapped by PSOCT imaging would be an improved indicator to contrast the WSLs without ambiguity. Here we show the ability of the local axis orientation to contrast the WSLs with clear boundaries even in the region with slight demineralization. Figure 5 shows the PSOCT imaging results of an intact, extracted human tooth (Fig. 5(A)), arranged in both cross-sectional and *en face* views. The *en face* views were obtained at a depth of $135\ \mu\text{m}$ from the surface.

To show the local axis orientation can provide a unique contrast for WSLs with clear boundaries along the depth direction, cross-sectional images (as indicated by the dashed line in Fig. 5(A))

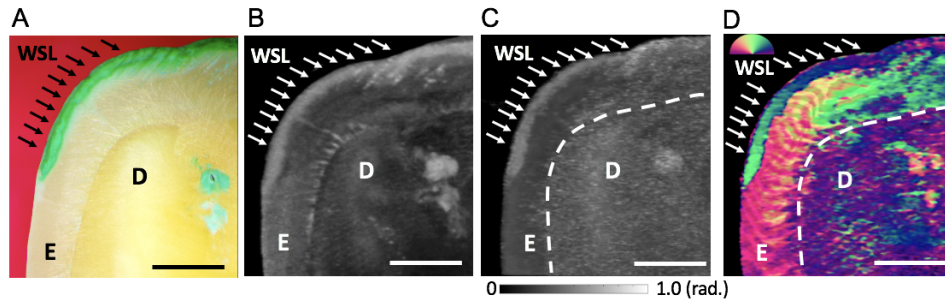


Fig. 4. Validation of the PSOCT mappings using the standard histological staining approach, sectioned in occlusal plane. (A) Photograph of the stained sectioned enamel. The WSLs are stained and visualized as a green color under the white light. A set of representative PSOCT *en face* images of the sectional surface, representing the contrasting parameters of (B) OCT scan, (C) local phase retardation and (D) local axis orientation derived from the human enamel, respectively. The orientation value of the WSLs is approximately orthogonal to the healthy enamel below the WSLs, along the radial axis, demonstrating the sign reversion of the WSLs. The contour of the WSLs in the PSOCT mapping are consistent with the staining result in (A). The *en face* images are at the depth of 30 μm . E: enamel; D: dentin. The scale bar = 1 mm.

were selected (Figs. 5(B)–5(E)). It is difficult to identify the boundary between the healthy enamel and the WSL in the depth direction from the intensity (Fig. 5(B)), DOPU (Fig. 5(C)) and local phase retardation (Fig. 5(D)) images. This is because different stages of demineralization can alter these three parameters in various degrees, leading to a difficulty to find a suitable threshold and boundary to extract the WSL. However, the WSL can be visualized without ambiguity in the local axis orientation image (Fig. 5(E)) simply due to the sharp 90-degree transition in the local axis orientation value where the WSL occurs.

In the *en-face* views, the regions of the WSLs can be visualized as higher intensity signals (Fig. 5(F)), lower DOPU signals (Fig. 5(G)), higher phase retardation signals (Fig. 5(H)) and purple orientation signals (Fig. 5(I)), which is consistent with the region of WSLs identified in the photograph (Fig. 5(A)). However, the boundaries between the WSLs and healthy enamel are not clear, particularly at the regions indicated by the red arrows in the intensity (Fig. 5(F)), DOPU (Fig. 5(G)) and phase retardation (Fig. 5(H)) images, where the contrast is very low between the sound enamel and demineralization zones. It is very likely that the degree of the demineralization in this boundary region is in the early stage, because it is located at the transition area from the sound enamel to WSLs. We calculated the mean values of OCT intensity, DOPU, local phase retardation and local axis orientation at the two regions located at each side of the boundary (indicated by the boxes in Fig. 5(F)), where the black box and the red box are in the regions of the sound enamel and the WSLs, respectively. It should be noted that the unit of local PhR is radium per depth. One pixel per depth represents 10 μm . These values are tabulated in Fig. 5(J), where it is clear that the mean intensity value (0.61 ± 0.02 , mean \pm std), the mean DOPU value (0.84 ± 0.02) and mean local phase retardation value (0.23 ± 0.01) of the WSLs in the red box are very close to those values in the sound enamel (vs. 0.68 ± 0.02 , 0.78 ± 0.03 , and 0.25 ± 0.01 , respectively). In this case, it would be difficult to set a threshold to differentiate WSLs from the healthy enamel by using either of these three parameters. However, local axis orientation provides a high and uniform contrast for WSLs even in the region with slight demineralization as shown in (Fig. 5(I)), where a $\sim 90^\circ$ change in the axis orientation value is observed. Such distinct contrast demonstrates its unique ability to detect lesions regardless of the demineralization degree, simply

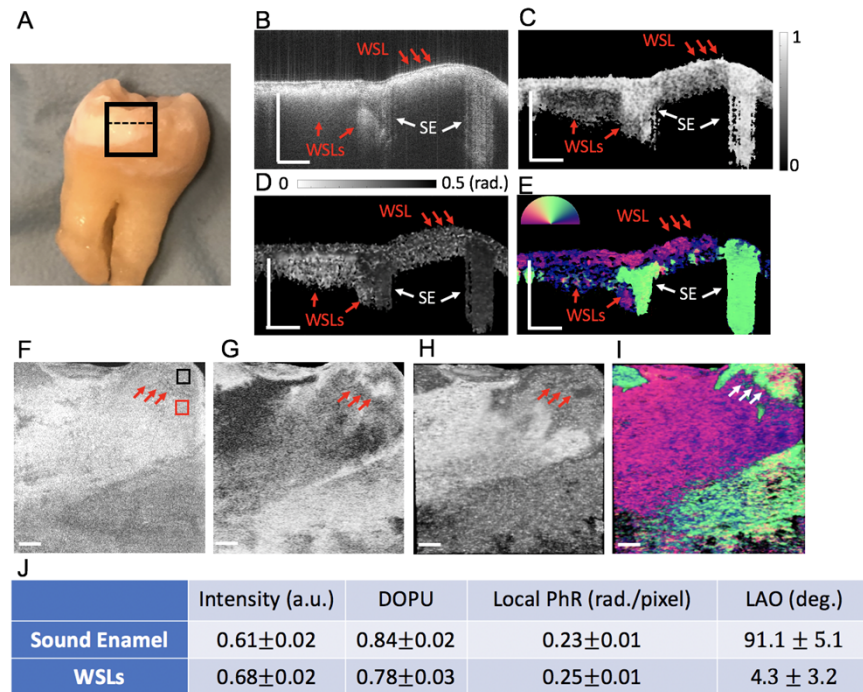


Fig. 5. PSOCT results of the human enamel with naturally formed WSLs. (A) Photograph of the human tooth with ICDAS score of 2, where the black box indicates the OCT scan region. The cross-sectional (B) intensity, (C) DOPU, (D) local phase retardation and (E) local axis orientation images derived from the human enamel, respectively. The red arrows in (B)-(E) indicate the WSLs while the white arrows indicate the sound enamel. (F)-(I) *En face* images of the enamel surface, representing (F) intensity, (G) DOPU, (H) local phase retardation and (I) local axis orientation, respectively. The arrows in (F)-(I) indicate the boundary between the WSLs and the sound enamel. The black and red box are located in the regions of the sound enamel and the WSLs respectively. (J) The table of the mean intensity, mean DOPU, mean local phase retardation and local axis orientation values (presented as mean \pm std) in the regions indicated by the two boxes respectively. SE: Sound enamel. The scale bar = 1 mm.

because the local axis orientation is only sensitive to the sign of the birefringence, which is a binary value.

3.2.3. Automatic segmentation of the WSLs using the local axis orientation

Because the sharp alteration in local axis orientation gives a clear boundary between WSLs and the healthy enamel, the local axis orientation can be used as an effective automatic segmentation tool to extract the three-dimensional WSL from healthy enamel. To demonstrate this idea, we selected an extracted human tooth with a ICDAS score of 2 (Fig. 6(A)) and performed 3D PSOCT scanning. The imaging FOV was 6 mm x 6 mm with 500 x 500 pixels. Figure 6 shows the segmentation results of the lesions in human enamel. Figure 6(B) shows the *en face* local axis orientation mapping of the human enamel at depth of 75 μ m below the surface, where the lesions are presented as a pink color while the green represents the healthy enamel, with the expected 90 degrees difference in axis orientation value. The contour of the pink color is consistent with the dark appearance in Fig. 6(A) that was identified as the caries by the expert clinician.

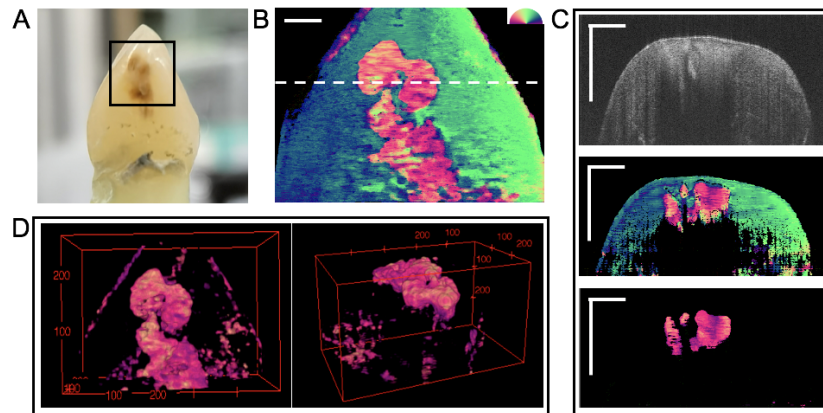


Fig. 6. Automatic segmentation of the lesions in human enamel using PS-OCT. (A) Photograph of the human tooth with ICDAS score of 2, where the black box indicates the OCT scan region. (B) The *en face* local axis orientation image of human enamel at depth of $\sim 75 \mu\text{m}$ below the surface. (C) The cross-sectional images derived from the human tooth at the position indicated by the white dashed line in (B): from top to the bottom represent the intensity, local axis orientation and the lesion segmentation images, respectively. (D) The 3D skeleton of the lesions in different angles of view. The scale bar = 1 mm.

Then the cross-sectional images of the tooth (indicated by the white dashed line in Fig. 6(B)) are presented in Fig. 6(C) to demonstrate the automatic segmentation strategy. The top image in Fig. 6(C) is the typical OCT structure image. Although the lesions can be differentiated as higher scattering signals, it demands manual efforts and advice from an experienced dentist to find an optimal threshold to segment the lesions from the healthy enamel. However, the sharp difference between WSLs and sound enamel provide clear boundaries of the lesions in the local axis orientation image (the middle image in Fig. 6(C)). This enables a simple green color-filter (Green value > 200) to automatically segment the lesions from the healthy enamel as shown in the bottom image in Fig. 6(C). Moreover, because of the 90 degrees contrast between the healthy enamel and the WSLs, the tolerance of the filter is large (i.e., the range of the optimal filter value is large), allowing this segmentation tool to be used in an effective and user-friendly way. By reconstructing the lesions in 3D, the skeleton of the lesions is extracted and visualized as shown in Fig. 6(D), which would enable the size, depth and morphology analyses of the lesions in the three dimensions. These results demonstrate the advantages of using the local axis orientation as the segmentation tool to extract the lesions from the healthy enamel.

4. Discussions and conclusion

Due to the porous nature of the enamel, the total measured birefringence of the enamel can be considered as a sum of two parts: 1) the negative intrinsic birefringence of the mineral material; 2) the positive form birefringence of the space between enamel crystals that is filled by non-mineral medium. In healthy enamel, the negative intrinsic birefringence dominates. During the demineralization process, the space between the enamel crystals becomes larger. When the size of the space (i.e., the pore volume) increases to a threshold, the positive birefringence dominates and reverses the sign of the total birefringence of the enamel from negative to positive [3,7]. It should be noted that the threshold is also related to the refractive index of the immersion media [34], hence the boundary formed by local axis orientation can be changed slightly with different immersion media. In this study, the tooth samples are all immersed within the deionized water. Further demineralization would lead to a higher positive birefringence. Therefore,

polarization-related techniques can distinguish the demineralization process by observing the reversal of negative to positive birefringence, and the increasing positive birefringence. In this study, an increase in the local phase retardation value and a sharp transition in the axis orientation ($\sim 90^\circ$) caused by the reversion of the sign of the birefringence have been detected in the WSLs, demonstrating that the PS-OCT can be used to detect these birefringence-induced effects in the WSLs in 3D space. Moreover, we found that the local axis orientation can give a unique contrast for the WSLs, enabling a simple and effective segmentation tool to segment and quantify the lesions in enamel.

A preserved layer above the lesions was reported in a prior study [3]. We did observe the preserved surface layer with appearance similar to sound enamel as shown in the middle image of Fig. 6(C). However, in the bovine enamel and the tooth used in Fig. 4 and Fig. 5, the preserved layer can only be seen in the polarization states images. In the polarization state results, the polarization state of the surface layer above the WSLs is the same as the sound enamel. We believe the layer is the preserved surface layer. However, because the phase retardation of the preserved surface layer and the sound enamel is relatively low, the depth of the preserved surface layer is not thick enough to make a visible change in the input polarization state. Hence, this layer was considered as the non-birefringent layer and was removed by using the color filter [26] in this study. This is the reason why the preserved layer was difficult to appreciate in the axis orientation images.

While we have demonstrated the usefulness of the local phase retardation and local axis orientation for the improved detection of WSLs in enamel, there are some limitations when using these two parameters to characterize the lesions. Firstly, severe depolarization effects induced by the lesions can affect the computation of the local phase retardation and local axis orientation because it can totally randomize the polarization states and hinder the computation of these two imaging parameters. In this case, the degree of depolarization uniformity may be the better choice for contrasting the lesions. Secondly, the local axis orientation value is also related to the geometry of the tooth. As shown in Fig. 4(D), the orientations of the enamel rods vary at different sites of the tooth rather than at a constant value. Hence, a geometrical correction relative to the tooth morphology should be applied to avoid the ambiguity and finally obtain the absolute birefringence sign mapping of the enamel. Thirdly, although the local axis orientation can contrast and determine the existence of the WSLs regardless of the demineralization degree, the tradeoff is that it cannot be used to grade the severity of the caries. On the contrary, other parameters like the DOPU value and local phase retardation may be correlated with the demineralization degree of the enamel, even though they provide relatively low contrast to differentiate WSLs from the healthy enamel. For example, as the degree of the demineralization increases, multiple scattering of the enamel will increase and lower the DOPU value. That is, the lower the DOPU value is, the more severe the demineralization would be. The signal attenuation in the OCT intensity image may also be used to reveal the degree of the multiple scattering and hence may be leveraged to indicate the stage of the demineralization. The same is true for the local phase retardation. The higher degree of the demineralization can increase the local phase retardation value. It should be noted that, although the intensity may be related to the degree of the multiple scattering, it may be challenging to use this OCT signal strength to grade the caries because it requires a constant light power impinging on the sample during the imaging, which is sometimes difficult in practice. In view of these considerations, a reasonable argument could be made to develop a multiple regression model (formulated by DOPU, OCT signal attenuation, phase retardation and optic axis orientation) to comprehensively identify and grade the severity of the caries lesion with improved accuracy.

The other limitation of this work is that the proposed method has not been validated in the *in vivo* study. There are two main differences between the *in vivo* study and the *in vitro* study of the enamel. When image the caries on the interproximal surfaces of the human tooth *in vivo*, the

incident direction of the probing light is no longer orthogonal to the surface of the enamel if there are adjacent teeth. Because the incident angle of the probing light relative to the birefringent sample can also affect the output polarization state of the light, the polarization measurement of the caries on the interproximal surfaces of the human tooth in vivo needs further exploration.

It should be noted that because the PSOCT system used in this study only utilized a single circularly polarized light to illuminate the sample, birefringent information could be lost under some special circumstances, for example where a first tissue layer transforms the (circular) input state to a linear state upon transmission. If the next layer has an optic axis aligned with this state, no polarization state evolution would result. A solution to mitigate this issue is to use two input polarization states in the implementation of the PSOCT system [11,12].

In summary, we have demonstrated the utility of the local axis orientation for contrast-enhanced mapping of WSLs in both bovine enamel and human teeth. A reversion in the sign of the birefringence in the WSLs has been investigated in some detail and can be uniquely mapped by the PSOCT measurement. We have also shown that this sign reversion in the birefringence provides a welcoming opportunity to automatically segment the lesions, enabling a 3D skeleton visualization. The local axis orientation mapping can provide fast and simple identification of WSLs before further statistical analysis and evaluation of the severity of the caries, which would be useful in the practical applications for the investigations of WSLs in enamel both pre-clinically and clinically.

Funding. Colgate-Palmolive Company; Washington Research Foundation; Department of Bioengineering, University of Washington; WRF David and Nancy Auth Innovation Award.

Acknowledgement. This study was supported in part by the Colgate Palmolive Company, Washington Research Foundation, and WRF David and Nancy Auth Innovation Award. Generous support from the Department of Bioengineering, University of Washington, is also acknowledged. The funding organization had no role in the design or conduct of this research. Portions of this work were included as part of the Ph.D. dissertation of Dr. Peijun Tang in 2021, "Development and Application of Polarization Sensitive Optical Coherence Tomography".

Ethics statement. The imaging of subjects reported in this study using laboratory-built investigational device was conducted in accordance with a protocol approved by the Institutional Review Board of the University of Washington and informed consent was obtained from all subjects. The study followed the tenets of the Declaration of Helsinki and was conducted in compliance with the Health Insurance Portability and Accountability Act.

Disclosures. Dr. Wang discloses intellectual property owned by the Oregon Health and Science University and the University of Washington. Dr. Wang also receives research support from Colgate Palmolive Company, Carle Zeiss Meditec Inc, and Facebook Technologies LLC. Dr. Kilpatrick-Liverman and Dr. Subhash are employees of Colgate Palmolive Company. All other authors have no disclosures.

Data availability. Data underlying the results presented in this paper are not publicly available at this time but may be obtained from the authors upon reasonable request.

References

1. S. Pathak, K. Roopa, P. Parameswarappa, and N. e, "White spot lesions: a literature review," *J. Pediatr. Dent.* **3**(1), 1–7 (2015).
2. J. D. B. J. C. D. Featherstone, "Prevention and reversal of dental caries: role of low level fluoride," *Commun Dent Oral Epidemiol* **27**(1), 31–40 (1999).
3. L. M. Silverstone, "Surface phenomena in dental caries," *Nature* **214**(5084), 203–204 (1967).
4. B. Angmar, D. Carlström, and J.-E. Glas, "Studies on the ultrastructure of dental enamel: IV. The mineralization of normal human enamel," *J. Ultrastruct. Res.* **8**(1-2), 12–23 (1963).
5. M. Wolman, "Polarized light microscopy as a tool of diagnostic pathology," *J. Histochem. Cytochem.* **23**(1), 21–50 (1975).
6. R. De Medeiros, J. Soares, and F. De Sousa, "Natural enamel caries in polarized light microscopy: differences in histopathological features derived from a qualitative versus a quantitative approach to interpret enamel birefringence," *J. Microsc.* **246**(2), 177–189 (2012).
7. H. S. M. Crabb and K. V. Mortimer, "Dental Caries and Enamel Structure," *Nature* **209**(5023), 611–612 (1966).
8. J. F. de Boer, C. K. Hitzenberger, and Y. Yasuno, "Polarization sensitive optical coherence tomography - a review [Invited]," *Biomed. Opt. Express* **8**(3), 1838–1873 (2017).
9. J. F. de Boer, T. E. Milner, M. J. C. van Gemert, and J. S. Nelson, "Two-dimensional birefringence imaging in biological tissue by polarization-sensitive optical coherence tomography," *Opt. Lett.* **22**(12), 934–936 (1997).

10. M. K. Al-Qaisi and T. Akkin, "Polarization-sensitive optical coherence tomography based on polarization-maintaining fibers and frequency multiplexing," *Opt. Express* **16**(17), 13032–13041 (2008).
11. M. Villiger, E. Z. Zhang, S. K. Nadkarni, W.-Y. Oh, B. J. Vakoc, and B. E. Bouma, "Spectral binning for mitigation of polarization mode dispersion artifacts in catheter-based optical frequency domain imaging," *Opt. Express* **21**(14), 16353–16369 (2013).
12. S. Makita, M. Yamanari, and Y. Yasuno, "Generalized Jones matrix optical coherence tomography: Performance and local birefringence imaging," *Opt. Express* **18**(2), 854–876 (2010).
13. P. Chen, Y. Chen, Y. Chen, Y. Yeh, K. Chang, M. Hou, and W. Kuo, "Quantification of structural and microvascular changes for diagnosing early-stage oral cancer," *Biomed. Opt. Express* **11**(3), 1244–1256 (2020).
14. P. Tang, M. A. Kirby, N. Le, Y. Li, N. Zeinstra, G. N. Lu, C. E. Murry, Y. Zheng, and R. K. Wang, and Applications, "Polarization sensitive optical coherence tomography with single input for imaging depth-resolved collagen organizations," *Light: Sci. Appl.* **10**(1), 1–12 (2021).
15. A. Motschi, P. Roberts, S. Desissaire, M. Schranz, F. Schwarzahans, H. Bogunović, M. Pircher, and C. Hitzenberger, "Identification and quantification of fibrotic areas in the human retina using polarization-sensitive OCT," *Biomed. Opt. Express* **12**(7), 4380–4400 (2021).
16. X. Zhou, S. Maloufi, D. Louie, N. Zhang, Q. Liu, T. Lee, and S. Tang, "Investigating the depolarization property of skin tissue by degree of polarization uniformity contrast using polarization-sensitive optical coherence tomography," *Biomed. Opt. Express* **12**(8), 5073–5088 (2021).
17. D. Zhu, J. Wang, M. Marjanovic, E. Chaney, K. Craddock, A. Higham, Z. Liu, Z. Gao, and S. Boppart, "Differentiation of breast tissue types for surgical margin assessment using machine learning and polarization-sensitive optical coherence tomography," *Biomed. Opt. Express* **12**(5), 3021–3036 (2021).
18. C. Liu, W. Ammon, R. Jones, J. Nolan, R. Wang, S. Chang, M. Frosch, A. Yendiki, D. Boas, C. Magnain, B. Fischl, and H. Wang, "Refractive-index matching enhanced polarization sensitive optical coherence tomography quantification in human brain tissue," *Biomed. Opt. Express* **13**(1), 358–372 (2022).
19. J. McBride, M. Hackmann, S. Nimphius, and B. Cense, "In vivo PS-OCT needle probe scan of human skeletal muscle," *Biomed. Opt. Express* **13**(3), 1386–1397 (2022).
20. E. Baradaran Shokouhi, R. Welch, K. Sivagurunathan, and A. Mandelis, "Multispectral truncated-correlation photothermal coherence tomography imaging modality for detection of early stage dental caries," *Biomed. Opt. Express* **13**(5), 2772–2781 (2022).
21. J. Golde, F. Tetschke, J. Walther, T. Rosenauer, F. Hempel, C. Hannig, E. Koch, and L. Kirsten, "Detection of carious lesions utilizing depolarization imaging by polarization sensitive optical coherence tomography," *J. Biomed. Opt.* **23**(07), 1 (2018).
22. C. Lee, C. L. Darling, and D. Fried, "Polarization-sensitive optical coherence tomographic imaging of artificial demineralization on exposed surfaces of tooth roots," *Dent. Mater.* **25**(6), 721–728 (2009).
23. R. C. Lee, H. Kang, C. L. Darling, and D. Fried, "Automated assessment of the remineralization of artificial enamel lesions with polarization-sensitive optical coherence tomography," *Biomed. Opt. Express* **5**(9), 2950–2962 (2014).
24. H. Kang, C. L. Darling, and D. Fried, "Nondestructive monitoring of the repair of enamel artificial lesions by an acidic remineralization model using polarization-sensitive optical coherence tomography," *Dent. Mater.* **28**(5), 488–494 (2012).
25. J. Walther, J. Golde, L. Kirsten, F. Tetschke, F. Hempel, T. Rosenauer, C. Hannig, and E. Koch, "In vivo imaging of human oral hard and soft tissues by polarization-sensitive optical coherence tomography," *J. Biomed. Opt.* **22**, 1–17 (2017).
26. P. Tang, J. Xu, and R. K. Wang, "Imaging and visualization of the polarization state of the probing beam in polarization-sensitive optical coherence tomography," *Appl. Phys. Lett.* **113**(23), 231101 (2018).
27. P. H. Tomlins and R. K. Wang, "Theory, developments and applications of optical coherence tomography," *J. Phys. D: Appl. Phys.* **38**(15), 2519–2535 (2005).
28. S. Makita, Y.-J. Hong, M. Miura, and Y. Yasuno, "Degree of polarization uniformity with high noise immunity using polarization-sensitive optical coherence tomography," *Opt. Lett.* **39**(24), 6783–6786 (2014).
29. P. Tang and R. Wang, "Polarization state tracing method to map local birefringent properties in samples using polarization sensitive optical coherence tomography," *Biomed. Opt. Express* **11**(12), 6852–6863 (2020).
30. R. K. Wang and Z. Ma, "A practical approach to eliminate autocorrelation artefacts for volume-rate spectral domain optical coherence tomography," *Phys. Med. Biol.* **51**(12), 3231–3239 (2006).
31. J. D. B. Featherstone and D. T. Zero, "An in situ model for simultaneous assessment of inhibition of demineralization and enhancement of remineralization," *J. Dent. Res.* **71**(3_suppl), 804–810 (1992).
32. N. Pitts, "'ICDAS' - An international system for caries detection and assessment being developed to facilitate caries epidemiology, research and appropriate clinical management," *Community Dent. Health* **21**, 193–198 (2004).
33. D. F. G. Poole, K. V. Mortimer, A. I. Darling, and W. D. Ollis, "Molecular sieve behaviour of dental enamel," *Nature* **189**(4769), 998–1000 (1961).
34. F. Sousa, S. Vianna, and N. Santos-Magalhaes, "Dental enamel birefringence for a wide mineral content range and for different immersion media's refractive indexes: An improved mathematical interpretation," *J. Microsc.* **233**(1), 69–75 (2009).